Ballistic thermal phonons traversing nanocrystalline domains in oriented polyethylene

Andrew B. Robbins[a], Stavros X. Drakopoulos[b], Ignacio Martin-Fabiani[b], Sara Ronca[b,1], and Austin J. Minnich[a,1]

[a]Division of Engineering and Applied Science, California Institute of Technology, Pasadena, CA 91125; and [b]Department of Materials, Loughborough University, Loughborough LE11 3TU, United Kingdom

Thermally conductive polymer crystals are of both fundamental and practical interest for their high thermal conductivity that exceeds that of many metals. In particular, polyethylene fibers and oriented films with uniaxial thermal conductivity exceeding 50 W·m^{-1}·K^{-1} have been reported recently, stimulating interest into the underlying microscopic thermal transport processes. While ab initio calculations have provided insight into microscopic phonon properties for perfect crystals, such properties of actual samples have remained experimentally inaccessible. Here, we report the direct observation of thermal phonons with mean free paths up to 200 nm in semicrystalline polyethylene films using transient grating spectroscopy. Many of the mean free paths substantially exceed the crystalline domain sizes measured using small-angle X-ray scattering, indicating that thermal phonons propagate ballistically within and across the nanocrystalline domains; those transmitting across domain boundaries contribute nearly one-third of the thermal conductivity. Our work provides a direct determination of thermal phonon propagation lengths in molecular solids, yielding insights into the microscopic origins of their high thermal conductivity.

polymers | polyethylene | thermal conductivity | mean free path | ballistic transport

Thermal conduction in oriented polymers is of intense interest as their thermal conductivities rival those of many covalent solids (1–4). While unoriented polymers typically exhibit isotropic and low thermal conductivity, κ, on the order of 0.2 W·m^{-1}·K^{-1} (5), oriented polymers may have uniaxial thermal conductivity orders of magnitude larger due to conduction via stiff covalent bonds along the polymer backbone and phonon focusing effects (6). Early studies of the κ of polymers reported enhancements in oriented amorphous polymers (7) and oriented semicrystalline polymers like polyethylene (8–10) and polypropylene (2). Since then, numerous works have examined the many factors contributing to increased κ in a variety of oriented polymers, including amorphous polymers (11, 12), polyethylene (1, 3, 6, 13–19), polyacetylene (20), and polymer fibers like Kevlar (21).

Semicrystalline polyethylene (PE) has received the most attention due to its ease of crystallization and stability. Bulk PE is naturally semicrystalline, composed of amorphous and crystalline domains with random orientation (1). When stretched to a draw ratio (DR) of around 10, the increased alignment of the individual crystalline domains along the draw direction can improve κ by a factor of at least 20 (9, 10, 16, 18). Oriented amorphous domains can also contribute to increased thermal conductivity (1, 14) and at ultrahigh draw ratios exceeding ~40, growth in the crystalline domain size can lead to further increases (17, 18, 22). The highest thermal conductivities reported in bulk samples with draw ratios exceeding 100 are around 65 W·m^{-1}·K^{-1} (18, 23).

The exceptional thermal conductivities of these materials have driven interest in the microscopic properties of the phonons transporting heat. These microscopic properties, such as the phonon mean free paths (MFPs), are typically inaccessible to conventional thermal characterization methods as they yield observables that average over the phonon distribution. As a result, theoretical studies have sought to obtain this information

using atomistic simulations such as molecular dynamics (3, 24–26) or ab initio calculations (27, 28). A recent work reported an ab initio calculation of the κ of a perfect PE crystal accounting for quantum nuclear motion, predicting an upper bound of 164 W·m^{-1}·K^{-1} at room temperature (28). The corresponding MFPs were predicted to be in the range of 10 nm to 1 µm. However, ab initio calculations assume perfect crystals, and actual samples are far more complex. For example, PE contains a nonnegligible amorphous fraction spread among the crystalline domains. These crystallites generally have thicknesses on the order of 10 nm to 75 nm immediately after synthesis (29–32). The precise size of crystalline domains and their dependence on sample orientation can depend on numerous factors such as molecular weight, sample fabrication, and any postprocessing such as rolling and stretching (18, 22). These imperfections may lead to additional phonon scattering, and therefore the actual MFPs in semicrystalline PE are likely different from ab initio predictions for a perfect crystal.

The discrepancy between the perfect crystals of ab initio calculations and actual samples is best bridged by experiments that can resolve microscopic heat transport properties. Mean free path spectroscopy is now an established technique to obtain this microscopic information by observing heat conduction over length scales comparable to MFPs using an appropriate experimental method (33–35). In particular, transient grating (TG) spectroscopy is capable of performing the required

Significance

Polymer crystals that are good conductors of heat are highly desirable for thermal management applications. Although thermally conductive polymer crystals are well known, the microscopic thermal transport processes that enable these properties have been challenging to probe experimentally. We used an optical method to probe heat conduction at submicrometer length scales, allowing us to obtain the distribution of mean free paths of heat carriers in oriented polyethylene. Our work provides key experimental insight into thermal transport in molecular solids that will aid in the synthesis of materials with higher thermal conductivity.

measurements on thin films at submicrometer length scales (36). However, this technique has not yet been applied to any polymer, and the MFPs of phonons in semicrystalline PE samples remain unknown.

In this work, we report the direct observation of thermal phonons with MFPs as high as 200 nm in oriented semicrystalline PE using TG. The MFPs are comparable to or exceed crystalline domain sizes measured with small-angle X-ray scattering, indicating that phonons propagate ballistically within and across the nanocrystalline domains. Our work reveals the MFPs of thermal phonons in molecular solids and demonstrates a general route to probe the microscopic phonon transport processes in crystalline polymers.

Results

Transient Grating Spectroscopy. We used TG (36–42) to observe heat conduction in the plane of PE films over micrometer length scales. In our implementation of this optical method, a pair of pump laser pulses are interfered on a sample at angle θ, creating a sinusoidal temperature profile with period d as shown in Fig. 1A. A continuous-probe laser diffracts from the thermal grating and is overlapped with a reference beam; the intensity of this probe signal is then monitored in time. The rate of decay of the signal provides information on the thermal transport properties of the sample. The pump and probe are focused to ensure a 4-beam overlap using a phase mask and 2 lenses, as shown in Fig. 1B. Additional experimental details are provided in *Materials and Methods*.

Samples were made by compression molding of nascent disentangled ultrahigh molecular weight PE (UHMWPE), further uniaxially rolled in a calender below the melting temperature (*Materials and Methods* and *SI Appendix*, section S1). Fig. 1C shows a typical PE sample, which incorporates a small concen-

tration of ZnO. As TG requires the sample to absorb light at visible wavelengths, and because PE is almost entirely transparent at such wavelengths, trace amounts of fillers were introduced before molding (see *Materials and Methods* for more information). ZnO nanoparticles (NPs) and beta-carotene were both used in different samples and found to be stable.

Fig. 1C shows a representative transient measurement on a PE film measured at a grating period of $d = 5.4\,\mu m$. The signal follows a single exponential decay with a decay time $\tau = (\alpha q^2)^{-1}$, where α is the thermal diffusivity and $q = 2\pi d^{-1}$ is the grating wavevector. The thermal conductivity is calculated from the diffusivity using literature values for the heat capacity of semicrystalline PE (43). Because thermal transport occurs along a single direction defined by the grating, the measured thermal conductivity of highly anisotropic semicrystalline PE varies with in-plane rotation angle. Fig. 1D shows the angle-dependent thermal conductivity measurement for PE with a draw ratio of 7.5, with a maximum value of 9.3 W·m^{-1}·K^{-1}. Similar values for comparable draw ratios were measured by laser-flash thermal analysis (18), thus suggesting that the presence of low amounts of either ZnO or beta-carotene does not significantly affect the thermal conductivity value. This result should be expected considering that the filler will reside only in the amorphous phase and, at the low draw ratio examined, the thermal conductivity will be mainly dependent on the orientation of the crystalline domains. The presence of particles in oriented amorphous domains may become relevant at higher draw ratios.

Quasiballistic Heat Transport in Polyethylene. The grating period on the sample can be tuned by changing the interference angle, θ. When d is small enough relative to the MFPs, heat transport occurs quasiballistically rather than diffusively (34, 36, 44–46). However, the MFPs of PE samples are likely smaller compared
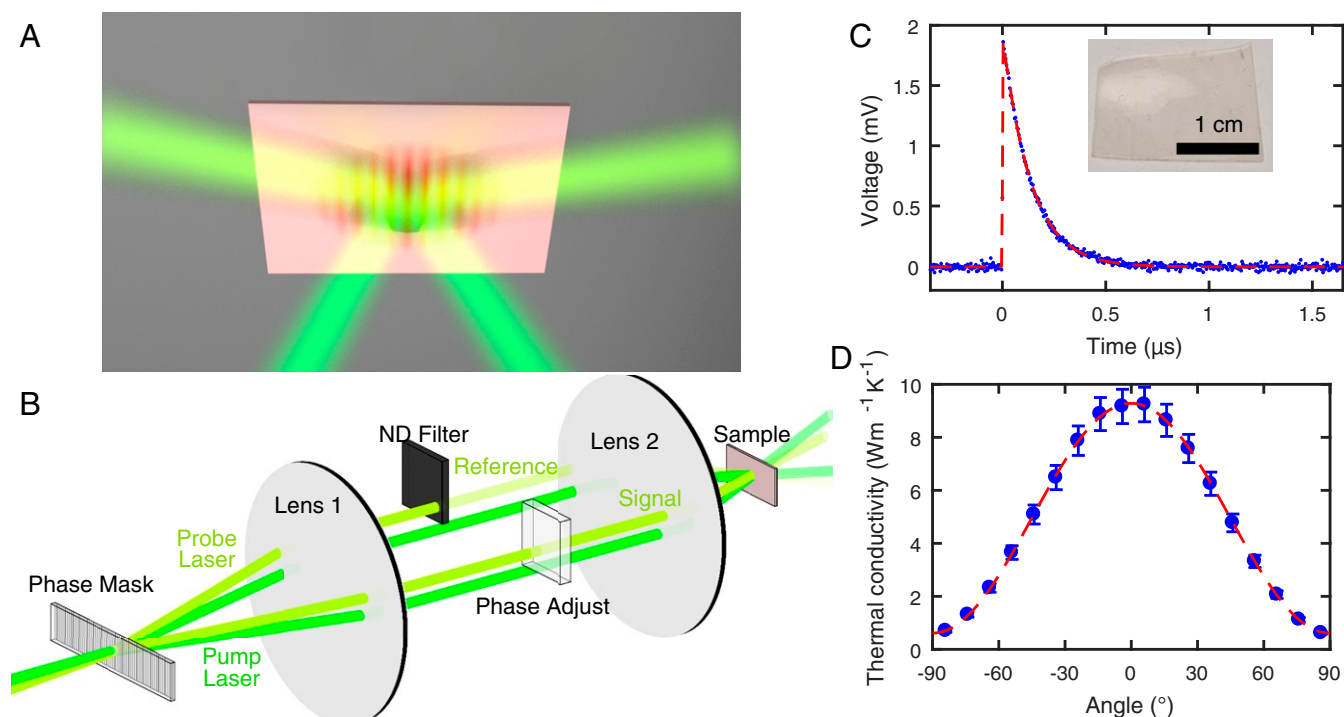

Fig. 1. TG schematics and measurements on PE film. (A) Schematic of the pump beams forming an optical grating in a TG experiment and the probe beams diffracting from it. (B) Diagram of the TG optical setup. Pump and probe beams are split at the phase mask, collimated by a pair of lenses, and focused onto the sample to form the grating pattern. (C) Measured signal vs. time for DR7.5 using a grating period of 5.4 μm. *Inset* shows optical image of a drawn polyethylene film (DR5). (D) In-plane thermal conductivity vs. angle relative to the film drawing direction for DR7.5. Error bars represent 95% confidence intervals. Uncertainty analysis is discussed in *Materials and Methods*.

with those probed in prior works (36), and so we need to access smaller grating periods. We use large-diameter aspherical lenses that support large values of $\theta > 20°$ and thus enable grating periods d on the sample ranging from 577 nm to 15.7 μm. Quasiballistic effects lead to the measured thermal conductivity differing from the bulk value and appearing to depend on the grating period (34, 36, 44–46). Prior work has established that the thermal conductivity accumulation function vs. MFP can be extracted from these measurements by solving an inverse problem (47).

We measured the apparent thermal conductivity κ vs. grating period for PE films with a DR = 2.5, 5, and 7.5, denoted as DR2.5, DR5, and DR7.5, all shown in Fig. 2. The measured κ for DR2.5 shows the thermal conductivity is nearly independent of grating period, indicating that MFPs are all smaller than the minimum thermal length scale accessible in the experiment. However, for DR5, κ exhibits a modest decrease below 1 μm. Finally, for DR7.5, the thermal conductivity is nearly double those of the other samples and exhibits a clear grating period dependence, with a noticeable decrease below 1.5 μm. This trend provides direct experimental evidence of ballistic thermal phonons over the thermal scale defined by the grating period (36, 40, 47). From the observed decrease in κ, we can roughly estimate (47, 48) that phonons with MFPs as high as $\sim d/2\pi \approx 200$ nm exist, although a quantitative analysis will follow. It is notable that these ballistic phonons are present in samples with relatively small DR and substantial microstructural imperfections.

We next use the experimental data to obtain the thermal conductivity accumulation vs. MFP, $F(\Lambda)$, where Λ is the component of the MFP in the measurement direction. This function can be obtained from measurements by solving an inverse problem (47, 48). However, the inverse problem is essentially a deconvolution, an ill-posed problem, and thus lacks a unique solution. To overcome this difficulty, we use Bayesian inference and a Metropolis–Hastings Markov chain Monte Carlo algorithm to quantify a posterior distribution and credible interval for $F(\Lambda)$ (42, 49). The method finds distributions of $F(\Lambda)$ that reproduce the measured data while also imposing a prior that incorporates physical knowledge of the solution. Here, the physical constraint
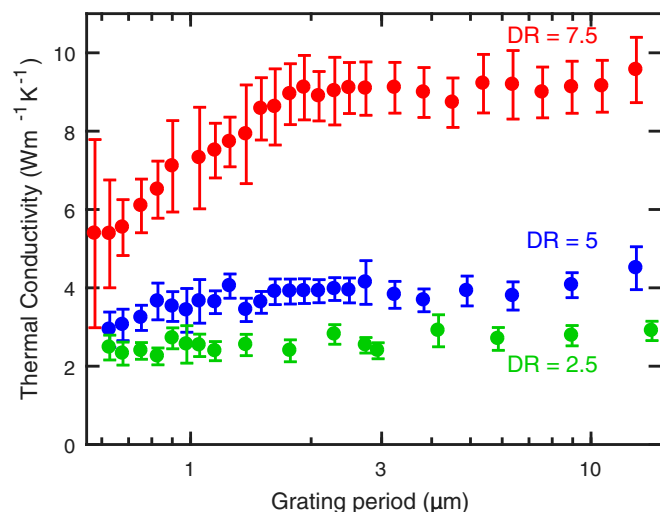
encoded in the prior is that $F(\Lambda)$ is a smooth function. Details on the algorithm and its implementation can be found in *SI Appendix*, section S4.

The inputs to this algorithm are the measured thermal conductivities for DR5 and DR7.5. For each dataset, we perform Bayesian inference to obtain a posterior distribution and a credible interval for $F(\Lambda)$. The reconstructed MFP spectra for each sample are given in Fig. 3A. The intensity in the plot is directly proportional to the probability distribution for $F(\Lambda)$. The solid lines correspond to the mean of the posterior distributions for each sample, and the dashed lines show the respective 95% credible intervals for the distributions. The predicted thermal conductivity vs. grating period from Bayesian inference for each sample is overlaid on the measured data in Fig. 3B, demonstrating good agreement.

These results provide quantitative microscopic insight into the properties of the thermal phonons transporting heat. We first consider DR5 and examine how much of the thermal conductivity contribution is due to phonons with MFPs above 90 nm. Fig. 3A shows that 11% of the contributed thermal conductivity is due to phonons with MFPs exceeding 90 nm according to the mean MFP distribution, while that for DR7.5 is 39%. The uncertainty can be quantified from the 95% credible interval of the posterior distribution, which gives a range from 0% to 24% for DR5 and from 23% to 53% for DR7.5. Even with the given uncertainties, the MFPs of phonons carrying heat are clearly larger in DR7.5, with some MFPs up to 200 nm.

To place these results in context, we compare them with prior estimations and calculations for polymer crystals. Our measured MFPs are far longer than prior estimates based on anisotropic kinetic theory (6, 21), which predicted MFPs of only tens of nanometers. We additionally compare our results with a recent ab initio calculation for a perfect PE crystal, which reported a κ of 164 W·m^{-1}·K^{-1} (28) at room temperature. While the magnitude of the conductivities is clearly very different, owing to the different microstructures considered in each case, the calculations predict the MFPs in the range of 10 nm to 1 μm, with significant contributions from phonons with MFPs on the order of 100 nm. The typical MFPs contributing to thermal conduction obtained here are in the same general range but shorter, mostly less than 200 nm, as expected from structural and defect scattering in a semicrystalline, partial aligned sample.

Microstructure Characterization of Polyethylene Samples. We next seek to place these measurements in context with the microstructural properties of the samples. Measurements of the temperature dependence on thermal conductivity can provide insight into the dominant scattering mechanism and thereby provide evidence of the impact of structural disorder. We conducted temperature-dependent measurements of κ with a grating period of 6.4 μm so that heat conduction occurs by diffusion for DR7.5. The results, given in Fig. 4A, exhibit an increasing trend characteristic of thermal conductivity limited by structural disorder. Note that the nonmonotonic region near 200 K overlaps with the glass transition temperature of amorphous PE (50, 51).

These measurements suggest that structural disorder is the dominant scattering mechanism. As is well known, oriented PE has a microstructure consisting of crystallites surrounded by amorphous regions, with crystal domain sizes typically ranging from 10 nm to 75 nm (29–32). Diffuse phonon reflections may be expected to occur at the domain boundaries, leading to a temperature-independent scattering mechanism that is qualitatively consistent with the temperature dependence of the thermal conductivity.

To characterize these microstructural features, we first used small-angle X-ray scattering (SAXS) to measure the average crystalline size. Fig. 4B shows curves for 3 PE films prepared

Fig. 2. Quasiballistic thermal transport in polyethylene films. Shown is thermal conductivity vs. grating period for DR2.5, DR5, and DR7.5. No significant dependence on grating period is observed for DR2.5, but clear decreases in the apparent κ with decreasing grating period are observed in DR5 and DR7.5, indicating the presence of ballistic phonons. As the draw ratio increases, both the maximum thermal conductivity and grating-dependent trend increase. Error bars represent 95% confidence intervals. Uncertainty analysis is discussed in *Materials and Methods* (55).
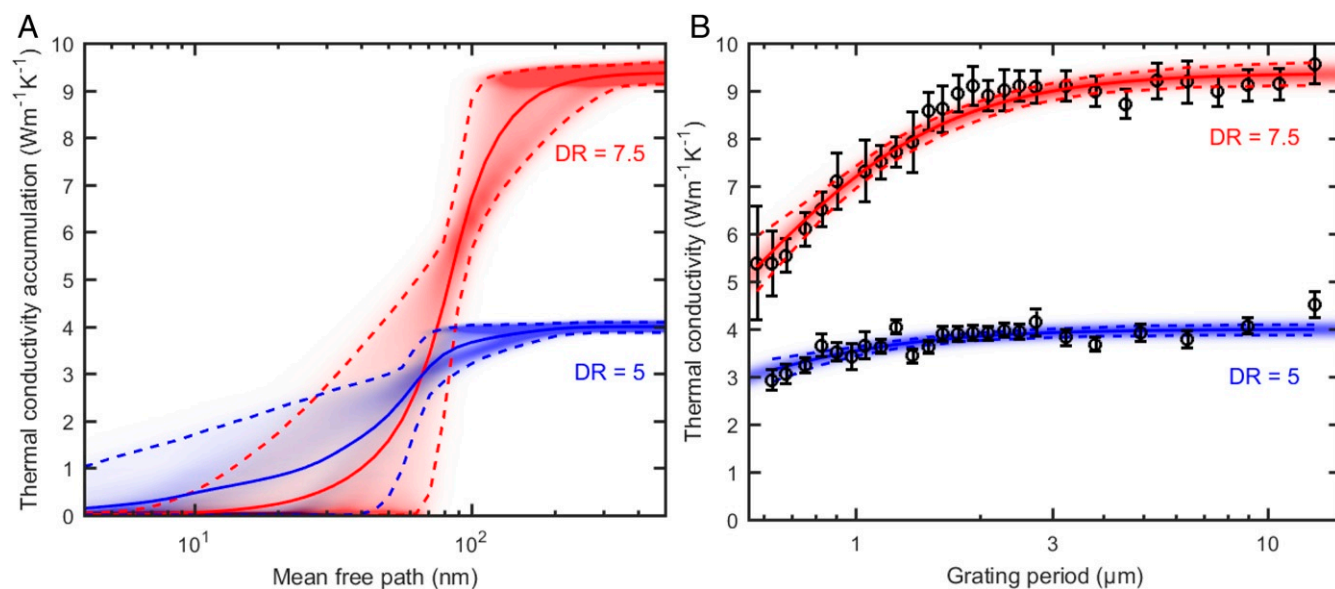
Fig. 3. MFP reconstruction for PE samples. (*A*) Posterior probability distribution of reconstructed MFP spectra from (red) DR7.5 and (blue) DR5 PE films. The intensity of the shaded regions corresponds to probability density, reflecting the likelihood that the accumulation function passes through that region. The solid lines represent the mean MFP spectra. The dashed lines correspond to the 95% credible interval. Phonons with MFPs on the order of 100 nm contribute substantially to heat conduction. (*B*) Thermal conductivity vs. grating period along with the calculated grating-dependent thermal conductivity corresponding to the posterior distributions of the MFP spectra from *A*.

at the same time as the present samples, corresponding to the same draw ratios and ZnO nanoparticles as the filler, obtained through azimuthal integration of the 2D SAXS patterns (Fig. 4 *B*, *Insets*). The results are consistent for the various samples prepared for this work and indicate that over the range of draw ratios studied, the average lamellar spacing ($d = 2\pi q^{-1}$) is on the order of 35 nm to 50 nm in the direction of the oriented chains, with only a slight increase over this range of draw ratios. Corresponding wide-angle X-ray scattering (WAXS) measurements (*SI Appendix*, Figs. S1 and S2) indicate that the crystallinity is

in the range of 70% to 80% and increases with increasing draw ratio. The orientation of PE chains in the stretching direction was found to increase with increasing draw ratios, as indicated by the decrease in the full width at half maximum of the (200) reflection (*SI Appendix*, Fig. S2). These observations provide an explanation for the increase in crystal size and therefore lamellar spacing observed by SAXS as the samples are stretched further. A distribution of the lamellar spacing was estimated from Fig. 4*B* by fitting a log-normal distribution to the DR = 7.5 sample data. This procedure yielded a SD of ~10 nm. Taking this
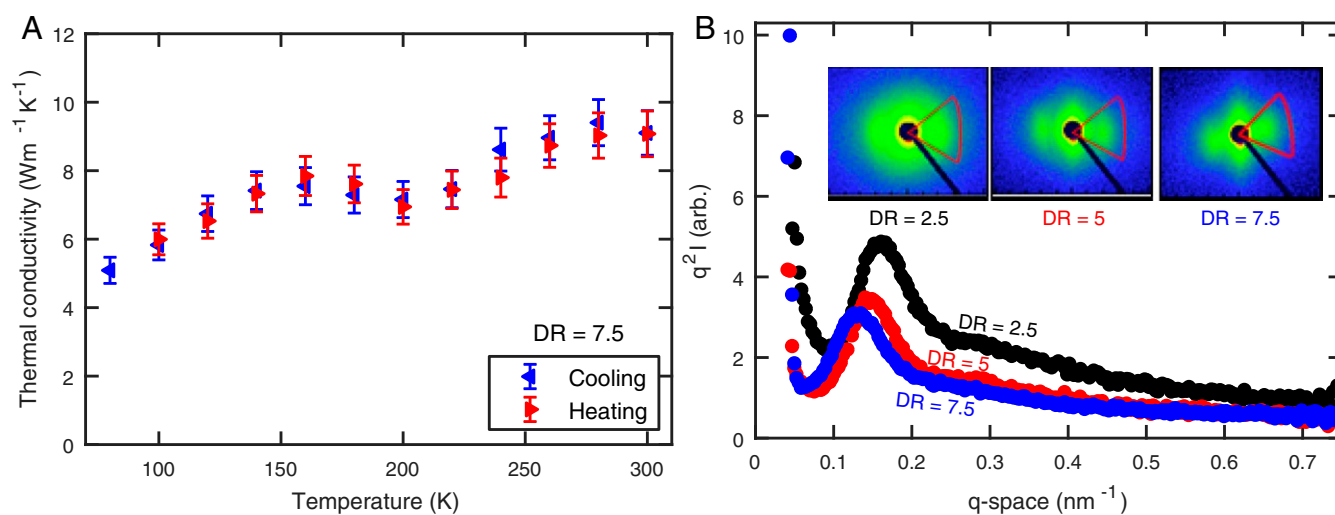

Fig. 4. Temperature-dependent thermal conductivity and SAXS measurements of PE film. (*A*) Thermal conductivity vs. temperature for DR7.5 with $d = 6.4\ \mu m$. An increase in thermal conductivity with increasing temperature is observed, indicating scattering dominated by structural disorder. The bump around 200 K corresponds to the glass transition of polyethylene (50, 51). (*B*) Lorentz-corrected SAXS curves for PE films filled with ZnO NPs and stretched at DRs = 2.5, 5, and 7.5. These curves are obtained from the azimuthal integration of the corresponding 2D SAXS patterns (*Insets*) over the sector where the lamellar spacing signal can be detected (drawn in red). The stretching direction corresponds to the horizontal direction (equator) in the images. From the main peak in the corrected SAXS curves, the average distance between crystalline lamellae can be estimated as $d = 2\pi/q$, being 40.5 nm, 42.3 nm, and 47.3 nm for draw ratios 2.5, 5.0, and 7.5, respectively (55, 56).

value as an estimate of the size distribution of the crystallites, the results indicate that the crystalline domain sizes likely do not exceed 60 nm.

Discussion

Considering these results, we can draw 2 primary conclusions. First, based on the temperature-dependent thermal conductivity, it is apparent that structural scattering dominates in our samples. This conclusion is further supported by the MFP and SAXS measurements, which found that a majority of phonon MFPs were on the order of the crystalline domain size. Together, these results indicate that domain boundary scattering is the dominant mechanism limiting thermal conductivity rather than phonon–phonon scattering or atomic defect scattering.

Second, despite the dominance of boundary scattering, our results suggest that a nonnegligible fraction of phonons are able to transmit across domain boundaries and traverse multiple grains, as evidenced by the portions of the MFP spectrum in Fig. 3A well above the upper limit to the crystal domain sizes of ~60 nm. For DR7.5, this fraction is at least 45% for phonon MFPs exceeding 60 nm. While the precise structure of the interface between amorphous and crystalline regions is unclear, this result suggests that the amorphous regions, which are also oriented, are able to support the propagation of low-energy thermal phonons despite their lack of crystalline order. Increases in thermal conductivity of oriented amorphous polymers have been observed (1, 7, 11, 12, 14); however, the microscopic transport processes of thermal phonons at amorphous–crystalline boundaries remain poorly understood. Our results provide evidence that the amorphous regions support the propagation of some thermal phonons and transmit them between crystalline regions. This contribution from phonons transmitting through amorphous regions is a substantial portion of the total thermal conductivity; for example, if the MFPs were limited to the grain size as is typically assumed, DR7.5 would have a reduction in thermal conductivity of nearly one-third.

Conclusion

In summary, we report direct measurements of the MFPs of thermal phonons in semicrystalline PE. Despite the relatively low draw ratio and crystallinity, phonons were found to propagate up to 200 nm. Microstructural analysis of the crystallite sizes indicates that phonons ballistically propagate within and across the nanocrystalline domains, suggesting that the amorphous regions can support the propagation of thermal phonons. Our work provides a direct experimental window into the microscopic transport processes in an oriented polymer and further demonstrates a general experimental route to study the microscopic transport properties of molecular solids.

Materials and Methods

Sample Fabrication. The ZnO NPs (particle size <100 nm, surface area between 15 mg^2·g^{-1} and 25 mg^2·g^{-1}, assay ~80%) and beta-carotene (assay >97%) were purchased from Sigma Aldrich and used as received. Nascent particles of disentangled UHMWPE were synthesized according to Rastogi et al. (22). M$_w$, calculated by means of melt plate–plate rheology (52), is 6.4 × 10^6 g·mol^{-1} and the molecular weight distribution (MWD) is 6.80. UHMWPE was suspended in acetone, and then either ZnO (suspended in acetone) or beta-carotene (dissolved in toluene) was added under stirring. The filler concentration was kept at 0.035% wt/wt for both. This small percentage minimizes any effect of the filler on the overall thermal properties, which was verified by comparing to previous results, measured by other means, that did not use fillers (18). Solvent was removed by evaporation overnight and samples were further dried at 50 °C in a vacuum oven

for 1 h. After compression molding (53), the sintered slabs were uniaxially oriented by means of twin rolling at a speed of 0.1 rpm. Both procedures were performed at 125 °C to retain a low entanglement density in the UHMWPE. The draw ratio of each sample was measured which, according to Ronca et al. (18), is the important quantity affecting thermal conductivity, rather than the choice of stretching. Rolled samples had a thickness on the order of 100 μm. We note that compression molding produces samples that are relatively optically smooth compared with some alternative methodologies such as stretching under uniaxial tension. Stretching under tension can produce striations in the resulting film that strongly scatter transmitted light, complicating measurement of the probe light in TG. Efforts to obtain usable TG signals from such samples are the subject of ongoing work.

SAXS and WAXS Experiments. Simultaneous SAXS and WAXS measurements were made using a Xenocs Xeuss 2.0 equipped with a microfocus Cu Kα source collimated with Scatterless slits. The SAXS signal was measured using a Pilatus 300K detector with a pixel size of 0.172 mm × 0.172 mm. The distance between the detector and the sample was calibrated using silver behenate (AgC$_{22}$H$_{43}$O$_2$), giving a value of 247 cm.

WAXS was measured on a Pilatus 100K mounted at an angle of 36° to the beam direction at a distance of 162 mm. The magnitude of the scattering vector (q) is given by $q = 4\pi \sin \theta / \lambda$, where 2θ is the angle between the incident and scattered X-rays and λ is the wavelength of the incident X-rays. This gave a q range for the detector of 1.3 A^{-1} to 3.3 A^{-1}. An azimuthal integration was performed on the 2D scattering profile and the resulting data were corrected for the absorption and background from the sample holder. The full width at half maximum (FWHM) was calculated by radial integration over a narrow q range around the (200) reflection to obtain its azimuthal profile and fitted with a Lorentzian distribution. WAXS data are discussed in *SI Appendix*, section S2 (54).

TG and Data Analysis. A full description of the TG experiment can be found in prior work (36, 40, 41). The implementation described by Vega-Flick et al. (41) closely resembles the setup used in this work. In our setup, the pump laser used to generate the thermal grating is a Coherent FlareNX laser with wavelength $\lambda = 515$ nm, an ~ 1-ns pulse width, a pulse repetition rate of 200 Hz, and a maximum pulse energy of ~ 300 MJ. Pump energies are attenuated to 15 MJ for data collection to minimize steady heating, and the beam diameter is magnified to ~520 μm at the sample position. The probe laser is a continuous-wave (CW) Coherent Sapphire laser with wavelength $\lambda = 532$ nm and a maximum power of 330 mW. The power is set to 100 mW, and the beam is mechanically chopped with a duty cycle of 3.2% to minimize steady heating. The beam diameter at the sample is ~470 μm. Unless otherwise specified, all reported thermal conductivity values are along the draw direction, corresponding to 0°. The grating period d was tuned from 577 nm to 15.7 μm using a variety of phase masks with binary patterns ranging from 2.4 μm to 60 μm in period. The telescope lenses are large-diameter aspheres (Thorlabs AL100100 and AL100200). The actual grating periods formed on the samples were directly measured by burning the patterns into a heat-sensitive polymer and measuring the grating period under a microscope.

The relaxation of the thermal grating is described by a single exponential decay, with the decay time τ being given by $\tau = (\alpha q^2)^{-1}$, where α is the thermal diffusivity and q is the grating wavevector where $q = 2\pi d^{-1}$. Additional fitting details are provided in *SI Appendix*, section S3. Temperature-dependent experiments were conducted in a Janis ST-100 optical cryostat under vacuum with $P < 10^{-5}$ mbar.

Please contact the authors with questions about the data (54–56) and any associated analysis.

1. C. L. Choy, Thermal conductivity of polymers. *Polymer* **18**, 984–1004 (1977).
2. C. L. Choy, F. C. Chen, W. H. Luk, Thermal conductivity of oriented crystalline polymers. *J. Polym. Sci. Polym. Phys. Ed.* **18**, 1187–1207 (1980).
3. S. Shen, A. Henry, J. Tong, R. Zheng, G. Chen, Polyethylene nanofibres with very high thermal conductivities. *Nat. Nanotechnol.* **5**, 251–255 (2010).
4. T. Zhang, X. Wu, T. Luo, Polymer nanofibers with outstanding thermal conductivity and thermal stability: Fundamental linkage between molecular characteristics and macroscopic thermal properties. *J. Phys. Chem. C* **118**, 21148–21159 (2014).
5. J. E. Mark, *Physical Properties of Polymers Handbook* (Springer Science & Business Media, 2007).

6. D. B. Mergenthaler, M. Pietralla, Heat conduction in highly oriented polyethylene. *Z. für Phys. B Condens. Matter* **94**, 461–468 (1994).

7. B. D. Washo, D. Hansen, Heat conduction in linear amorphous high polymers: Orientation anisotropy. *J. Appl. Phys.* **40**, 2423–2427 (1969).

8. S. Burgess, D. Greig, The low-temperature thermal conductivity of polyethylene. *J. Phys. C Solid State Phys.* **8**, 1637–1648 (1975).

9. C. L. Choy, W. H. Luk, F. C. Chen, Thermal conductivity of highly oriented polyethylene. *Polymer* **19**, 155–162 (1978).

10. H. G. Kilian, M. Pietralla, Anisotropy of thermal diffusivity of uniaxial stretched polyethylenes. *Polymer* **19**, 664–672 (1978).

11. S. Gupta, J. D. Schieber, D. C. Venerus, Anisotropic thermal conduction in polymer melts in uniaxial elongation flows. *J. Rheol.* **57**, 427–439 (2013).

12. V. Singh *et al.*, High thermal conductivity of chain-oriented amorphous polythiophene. *Nat. Nanotechnol.* **9**, 384–390 (2014).

13. D. M. Finlayson, P. J. Mason, Structure scattering and the thermal conductivity of a semicrystalline polymer. *J. Phys. C Solid State Phys.* **18**, 1791 (1985).

14. T. Mugishima, Y. Kogure, Y. Hiki, K. Kawasaki, H. Nakamura, Phonon conduction in polyethylene. *J. Phys. Soc. Japan* **57**, 2069–2079 (1988).

15. B. Poulaert, J. C. Chielens, C. Vandenhende, J. P. Issi, R. Legras, Thermal conductivity of highly oriented polyethylene fibers. *Polym. Commun.* **31**, 148–151 (1990).

16. D. B. Mergenthaler, M. Pietralla, S. Roy, H. G. Kilian, Thermal conductivity in ultraoriented polyethylene. *Macromolecules* **25**, 3500–3502 (1992).

17. C. L. Choy, Y. W. Wong, G. W. Yang, T. Kanamoto, Elastic modulus and thermal conductivity of ultradrawn polyethylene. *J. Polym. Sci. Part B Polym. Phys.* **37**, 3359–3367 (1999).

18. S. Ronca, T. Igarashi, G. Forte, S. Rastogi, Metallic-like thermal conductivity in a lightweight insulator: Solid-state processed ultra high molecular weight polyethylene tapes and films. *Polymer* **123**, 203–210 (2017).

19. R. Shrestha *et al.*, Crystalline polymer nanofibers with ultra-high strength and thermal conductivity. *Nat. Commun.* **9**, 1664 (2018).

20. L Piraux, M. Kinany-Alaoui, J. P. Issi, D. Begin, D. Billaud, Thermal conductivity of an oriented polyacetylene film. *Solid State Commun.* **70**, 427–429 (1989).

21. X. Wang, V. Ho, R. A. Segalman, D. G. Cahill, Thermal conductivity of high-modulus polymer fibers. *Macromolecules* **46**, 4937–4943 (2013).

22. S. Rastogi, Y. Yao, S. Ronca, J. Bos, J. van der Eem, Unprecedented high-modulus high-strength tapes and films of ultrahigh molecular weight polyethylene via solvent-free route. *Macromolecules* **44**, 5558–5568 (2011).

23. Y. Xu *et al.*, Nanostructured polymer films with metal-like thermal conductivity. *Nat. Commun.* **10**, 1771 (2019).

24. A. Henry, G. Chen, High thermal conductivity of single polyethylene chains using molecular dynamics simulations. *Phys. Rev. Lett.* **101**, 235502 (2008).

25. J. Liu, R. Yang, Length-dependent thermal conductivity of single extended polymer chains. *Phys. Rev. B* **86**, 104307 (2012).

26. T. Zhang, T. Luo, Morphology-influenced thermal conductivity of polyethylene single chains and crystalline fibers. *J. Appl. Phys.* **112**, 094304 (2012).

27. X. Wang, M. Kaviany, B. Huang, Phonon coupling and transport in individual polyethylene chains: A comparison study with the bulk crystal. *Nanoscale* **9**, 18022–18031 (2017).

28. N. Shulumba, O. Hellman, A. J. Minnich, Lattice thermal conductivity of polyethylene molecular crystals from first-principles including nuclear quantum effects. *Phys. Rev. Lett.* **119**, 185901 (2017).

29. L. Lu, R. G. Alamo, L. Mandelkern, Lamellar thickness distribution in linear polyethylene and ethylene copolymers. *Macromolecules* **27**, 6571–6576 (1994).

30. C. Marega, A. Marigo, G. Cingano, R. Zannetti, G. Paganetto, Small-angle X-ray scattering from high-density polyethylene: Lamellar thickness distributions. *Polymer* **37**, 5549–5557 (1996).

31. H. Zhou, G. L. Wilkes, Comparison of lamellar thickness and its distribution determined from d.s.c., SAXS, TEM and AFM for high-density polyethylene films having a stacked lamellar morphology. *Polymer* **38**, 5735–5747 (1997).

32. D. Hansen, G. A. Bernier, Thermal conductivity of polyethylene: The effects of crystal size, density and orientation on the thermal conductivity. *Polym. Eng. Sci.* **12**, 204–208 (1972).

33. Y. K. Koh, D. G. Cahill, Frequency dependence of the thermal conductivity of semiconductor alloys. *Phys. Rev. B* **76**, 075207 (2007).

34. M. E. Siemens *et al.*, Quasi-ballistic thermal transport from nanoscale interfaces observed using ultrafast coherent soft X-ray beams. *Nat. Mater.* **9**, 26–30 (2010).

35. A. J. Minnich *et al.*, Thermal conductivity spectroscopy technique to measure phonon mean free paths. *Phys. Rev. Lett.* **107**, 095901 (2011).

36. J. A. Johnson *et al.*, Direct measurement of room-temperature nondiffusive thermal transport over micron distances in a silicon membrane. *Phys. Rev. Lett.* **110**, 025901 (2013).

37. M. D. Fayer, Dynamics of molecules in condensed phases: Picosecond holographic grating experiments. *Annu. Rev. Phys. Chem.* **33**, 63–87 (1982).

38. J. T. Fourkas, M. D. Fayer, The transient grating: A holographic window to dynamic processes. *Acc. Chem. Res.* **25**, 227–233 (1992).

39. A. Tokmakoff, W. F. Banholzer, M. D. Fayer, Thermal diffusivity measurements of natural and isotopically enriched diamond by picosecond infrared transient grating experiments. *Appl. Phys. A* **56**, 87–90 (1993).

40. A. A. Maznev, J. A. Johnson, K. A. Nelson, Onset of nondiffusive phonon transport in transient thermal grating decay. *Phys. Rev. B* **84**, 195206 (2011).

41. A. Vega-Flick *et al.*, Laser-induced transient grating setup with continuously tunable period. *Rev. Sci. Instrum.* **86**, 123101 (2015).

42. N. K. Ravichandran, H. Zhang, A. J. Minnich, Spectrally resolved specular reflections of thermal phonons from atomically rough surfaces. *Phys. Rev. X* **8**, 041004 (2018).

43. S. S. Chang, A. B. Bastul, Heat capacities of polyethylene from 2 to 360 K. I. Standard samples of linear and branched polyethylene whole polymer. *J. Res. Natl. Inst. Stand. Technol.* **77A**, 395–405 (1973).

44. L. Zeng *et al.*, Measuring phonon mean free path distributions by probing quasi-ballistic phonon transport in grating nanostructures. *Sci. Rep.* **5**, 17131 (2015).

45. Y. Hu, L. Zeng, A. J. Minnich, M. S. Dresselhaus, G. Chen, Spectral mapping of thermal conductivity through nanoscale ballistic transport. *Nat. Nanotechnol.* **10**, 701–706 (2015).

46. X. Chen, C. Hua, H. Zhang, N. K. Ravichandran, A. J. Minnich, Quasiballistic thermal transport from nanoscale heaters and the role of the spatial frequency. *Phys. Rev. Appl.* **10**, 054068 (2018).

47. A. J. Minnich, Determining phonon mean free paths from observations of quasiballistic thermal transport. *Phys. Rev. Lett.* **109**, 205901 (2012).

48. A. J. Minnich, Phonon heat conduction in layered anisotropic crystals. *Phys. Rev. B* **91**, 085206 (2015).

49. W. K. Hastings, Monte Carlo sampling methods using Markov chains and their applications. *Biometrika* **57**, 97–109 (1970).

50. G. T. Davis, R. K. Eby, Glass transition of polyethylene: Volume relaxation. *J. Appl. Phys.* **44**, 4274–4281 (1973).

51. C. L. Beatty, F. E. Karasz, The glass transition of linear polyethylene. *J. Macromol. Sci. Part C* **17**, 37–60 (1979).

52. A. Pandey, Y. Champouret, S. Rastogi, Heterogeneity in the distribution of entanglement density during polymerization in disentangled ultrahigh molecular weight polyethylene. *Macromolecules* **44**, 4952–4960 (2011).

53. S. X. Drakopoulos, G. C. Psarras, G. Forte, I. Martin-Fabiani, S. Ronca, Entanglement dynamics in ultra-high molecular weight polyethylene as revealed by dielectric spectroscopy. *Polymer* **150**, 35–43 (2018).

54. A. Robbins, S. Drakopoulos, I. Martin-Fabiani, S. Ronca, A. Minnich, Wide-angle X-ray scattering data from stretched UHMWPE samples. Loughborough University Repository. https://repository.lboro.ac.uk/articles/Wide-angle_X-ray_scattering_data_from_stretched_UHMWPE_samples/9033998. Deposited 24 July 2019.

55. A. Robbins, S. Drakopoulos, I. Martin-Fabiani, S. Ronca, A. Minnich, Transient Grating of Rolled Polyethylene Films. CaltechDATA. https://data.caltech.edu/records/1262. Deposited 24 July 2019.

56. A. Robbins, S. Drakopoulos, I. Martin-Fabiani, S. Ronca, A. Minnich, Small-angle X-ray scattering data from stretched UHMWPE samples. Loughborough University Repository. https://repository.lboro.ac.uk/articles/Small-angle_X-ray_scattering_data_from_stretched_UHMWPE_samples/9009716. Deposited 24 July 2019.